Overview of progress in European medium sized tokamaks towards an integrated plasma-edge/wall solution

PAPER • OPEN ACCESS

Overview of progress in European medium sized tokamaks towards an integrated plasma-edge/wall solution[a]

To cite this article: H. Meyer *et al* 2017 *Nucl. Fusion* **57** 102014

OPEN ACCESS
IOP Publishing | International Atomic Energy Agency
Nuclear Fusion
Nucl. Fusion **57** (2017) 102014 (15pp)
https://doi.org/10.1088/1741-4326/aa6084

Overview of progress in European medium sized tokamaks towards an integrated plasma-edge/wall solution[a]

H. Meyer[5], T. Eich[37], M. Beurskens[5,38], S. Coda[15], A. Hakola[55], P. Martin[8], J. Adamek[29], M. Agostini[8], D. Aguiam[30], J. Ahn[6], L. Aho-Mantila[55], R. Akers[5], R. Albanese[51], R. Aledda[11], E. Alessi[23], S. Allan[5], D. Alves[30], R. Ambrosino[52], L. Amicucci[44], H. Anand[15], G. Anastassiou[40], Y. Andrèbe[15], C. Angioni[37], G. Apruzzese[44], M. Ariola[52], H. Arnichand[6], W. Arter[5], A. Baciero[35], M. Barnes[42], L. Barrera[18,45], R. Behn[15], A. Bencze[56], J. Bernardo[30], M. Bernert[37], P. Bettini[8], P. Bilková[29], W. Bin[23], G. Birkenmeier[37], J.P.S. Bizarro[30], P. Blanchard[15], T. Blanken[16], M. Bluteau[14], V. Bobkov[37], O. Bogar[29], P. Böhm[29], T. Bolzonella[8], L. Boncagni[44], A. Botrugno[44], C. Bottereau[6], F. Bouquey[6], C. Bourdelle[6], S. Brémond[6], S. Brezinsek[20], D. Brida[37], F. Brochard[46], J. Buchanan[5], H. Bufferand[6], P. Buratti[44], P. Cahyna[29], G. Calabrò[44], Y. Camenen[2], R. Caniello[23], B. Cannas[11], A. Canton[8], A. Cardinali[44], D. Carnevale[53], M. Carr[5], D. Carralero[37], P. Carvalho[30], L. Casali[37], C. Castaldo[44], F. Castejón[35], R. Castro[35], F. Causa[44], R. Cavazzana[8], M. Cavedon[37], M. Cecconello[12], S. Ceccuzzi[44], R. Cesario[44], C.D. Challis[5], I.T. Chapman[5], S. Chapman[7], M. Chernyshova[28], D. Choi[15], C. Cianfarani[44], G. Ciraolo[6], J. Citrin[19], F. Clairet[6], I. Classen[19], R. Coelho[30], J.W. Coenen[20], L. Colas[6], G. Conway[37], Y. Corre[6], S. Costea[25], F. Crisanti[44], N. Cruz[30], G. Cseh[56], A. Czarnecka[28], O. D'Arcangelo[44], M. De Angeli[23], G. De Masi[8], G. De Temmerman[31], G. De Tommasi[51], J. Decker[15], R.S. Delogu[8], R. Dendy[5], P. Denner[20], C. Di Troia[44], M. Dimitrova[29], R. D'Inca[37], V. Dorić[54], D. Douai[6], A. Drenik[32,37], B. Dudson[57], D. Dunai[56], M. Dunne[37], B.P. Duval[15], L. Easy[5], S. Elmore[5], B. Erdös[27], B. Esposito[44], E. Fable[37], M. Faitsch[37], A. Fanni[11], N. Fedorczak[6], F. Felici[16], J. Ferreira[30], O. Février[6], O. Ficker[29], S. Fietz[37], L. Figini[23], A. Figueiredo[30], A. Fil[6], G. Fishpool[5], M. Fitzgerald[5], M. Fontana[15], O. Ford[38], L. Frassinetti[22], R. Fridström[22], D. Frigione[44], G. Fuchert[37], C. Fuchs[37], M. Furno Palumbo[8], S. Futatani[4], L. Gabellieri[44], K. Gałązka[28], J. Galdon-Quiroga[45], S. Galeani[53], D. Gallart[4], A. Gallo[6], C. Galperti[15,23], Y. Gao[20], S. Garavaglia[23], J. Garcia[6], A. Garcia-Carrasco[22], J. Garcia-Lopez[45], M. Garcia-Munoz[45], J.-L. Gardarein[2], L. Garzotti[5], J. Gaspar[2], E. Gauthier[6], P. Geelen[16], B. Geiger[37], P. Ghendrih[6], F. Ghezzi[23], L. Giacomelli[23], L. Giannone[37], E. Giovannozzi[44], C. Giroud[5], C. Gleason González[33], M. Gobbin[8], T.P. Goodman[15], G. Gorini[49], M. Gospodarczyk[53], G. Granucci[23], M. Gruber[37], A. Gude[37], L. Guimarais[30], R. Guirlet[6], J. Gunn[6], P. Hacek[29], S. Hacquin[6], S. Hall[5], C. Ham[5], T. Happel[37], J. Harrison[5], D. Harting[5], V. Hauer[33], E. Havlickova[5], T. Hellsten[22], W. Helou[6], S. Henderson[14], P. Hennequin[34], M. Heyn[26], B. Hnat[42], M. Hölzl[36],

[a] In the future we will refer to the author list of the paper as the EUROfusion MST1 Team.

D. Hogeweij[19], C. Honoré[34], C. Hopf[37], J. Horáček[29], G. Hornung[9], L. Horváth[27], Z. Huang[15], A. Huber[20], J. Igitkhanov[33], V. Igochine[37], M. Imrisek[29], P. Innocente[8], C. Ionita-Schrittwieser[25], H. Isliker[3], I. Ivanova-Stanik[28], A.S. Jacobsen[43], P. Jacquet[5], M. Jakubowski[38], A. Jardin[6], F. Jaulmes[19], F. Jenko[37], T. Jensen[43], O. Jeppe Miki Busk[43], M. Jessen[43], E. Joffrin[6], O. Jones[5], T. Jonsson[22], A. Kallenbach[37], N. Kallinikos[3], S. Kálvin[56], A. Kappatou[19,37], J. Karhunen[1], A. Karpushov[15], S. Kasilov[26], G. Kasprowicz[28], A. Kendl[25], W. Kernbichler[26], D. Kim[15], A. Kirk[5], S. Kjer[43], I. Klimek[12], G. Kocsis[56], D. Kogut[6], M. Komm[29], S.B. Korsholm[43], H.R. Koslowski[20], M. Koubiti[2], J. Kovacic[32], K. Kovarik[29,42], N. Krawczyk[28], J. Krbec[29], K. Krieger[37], A. Krivska[36], R. Kube[25], O. Kudlacek[8,37], T. Kurki-Suonio[1], B. Labit[15], F.M. Laggner[24], L. Laguardia[23], A. Lahtinen[50], P. Lalousis[21], P. Lang[37], P. Lauber[37], N. Lazányi[27], A. Lazaros[40], H.B. Le[15], A. Lebschy[37], J. Leddy[57], L. Lefévre[47], M. Lehnen[31], F. Leipold[43], A. Lessig[37], M. Leyland[57], L. Li[20], Y. Liang[20], B. Lipschultz[57], Y.Q. Liu[5], T. Loarer[6], A. Loarte[31], T. Loewenhoff[20], B. Lomanowski[13], V.P. Loschiavo[51], T. Lunt[37], I. Lupelli[5], H. Lux[5], A. Lyssoivan[36], J. Madsen[43], P. Maget[6], C. Maggi[5], R. Maggiora[41], M.L. Magnussen[43], J. Mailloux[5], B. Maljaars[16], A. Malygin[15], P. Mantica[23], M. Mantsinen[4,58], M. Maraschek[37], B. Marchand[50], N. Marconato[8], C. Marini[15], M. Marinucci[44], T. Markovic[29], D. Marocco[44], L. Marrelli[8], Y. Martin[15], J.R. Martin Solis[35], A. Martitsch[26], S. Mastrostefano[17,52], M. Mattei[51], G. Matthews[5], M. Mavridis[3], M.-L. Mayoral[5,18], D. Mazon[6], P. McCarthy[48], R. McAdams[5], G. McArdle[5], P. McCarthy[48], K. McClements[5], R. McDermott[37], B. McMillan[7], G. Meisl[37], A. Merle[15], O. Meyer[6], D. Milanesio[41], F. Militello[5], I.G. Miron[39], K. Mitosinkova[29], J. Mlynar[29], A. Mlynek[37], D. Molina[6], P. Molina[15], I. Monakhov[5], J. Morales[6], D. Moreau[6], P. Morel[34], J.-M. Moret[15], A. Moro[23], D. Moulton[5], H.W. Müller[37], F. Nabais[30], E. Nardon[6], V. Naulin[43], A. Nemes-Czopf[27], F. Nespoli[15], R. Neu[37], A.H. Nielsen[43], S.K. Nielsen[43], V. Nikolaeva[30], S. Nimb[43], M. Nocente[49], R. Nouailletas[6], S. Nowak[23], M. Oberkofler[37], M. Oberparleiter[10], R. Ochoukov[37], T. Odstrčil[37], J. Olsen[43], J. Omotani[5], M.G. O'Mullane[14], F. Orain[6,37], N. Osterman[32], R. Paccagnella[8], S. Pamela[5], L. Pangione[5], M. Panjan[32], G. Papp[37], R. Papřok[29], V. Parail[5], F.I. Parra[42], A. Pau[11], G. Pautasso[37], S.-P. Pehkonen[55], A. Pereira[35], E. Perelli Cippo[23], V. Pericoli Ridolfini[52], M. Peterka[29], P. Petersson[22], V. Petrzilka[29], P. Piovesan[8], C. Piron[8], A. Pironti[51], F. Pisano[11], T. Pisokas[3], R. Pitts[31], I. Ploumistakis[21], V. Plyusnin[30], G. Pokol[27], D. Poljak[54], P. Pölöskei[27], Z. Popovic[35], G. Pór[27], L. Porte[15], S. Potzel[37], I. Predebon[8], M. Preynas[15], G. Primc[32], G. Pucella[44], M.E. Puiatti[8], T. Pütterich[37], M. Rack[20], G. Ramogida[44], C. Rapson[37], J.Juul Rasmussen[43], J. Rasmussen[43], G.A. Rattá[35], S. Ratynskaia[22], G. Ravera[44], D. Réfy[56], M. Reich[37], H. Reimerdes[15], F. Reimold[20,37], M. Reinke[57], D. Reiser[20], M. Resnik[32], C. Reux[6], D. Ripamonti[23], D. Rittich[37], G. Riva[23], M. Rodriguez-Ramos[45], V. Rohde[37], J. Rosato[34], F. Ryter[37], S. Saarelma[5], R. Sabot[6], F. Saint-Laurent[6], M. Salewski[43], A. Salmi[55], D. Samaddar[5], L. Sanchis-Sanchez[45], J. Santos[30], O. Sauter[15], R. Scannell[5], M. Scheffer[16], M. Schneider[6,31], B. Schneider[25], P. Schneider[37], M. Schneller[37], R. Schrittwieser[25], M. Schubert[37], J. Schweinzer[37], J. Seidl[29], M. Sertoli[37], S. Šesnić[54], A. Shabbir[9], A. Shalpegin[6], B. Shanahan[57], S. Sharapov[5], U. Sheikh[15], G. Sias[11], B. Sieglin[37], C. Silva[30], A. Silva[30], M. Silva Fuglister[15], J. Simpson[5], A. Snicker[1], C. Sommariva[6], C. Sozzi[23], S. Spagnolo[8], G. Spizzo[8], M. Spolaore[8], T. Stange[38], M. Stejner Pedersen[43], I. Stepanov[9], J. Stober[37], P. Strand[10], A. Šušnjara[54], W. Suttrop[37], T. Szepesi[56], B. Tál[56],

T. Tala[55], P. Tamain[6], G. Tardini[37], M. Tardocchi[23], A. Teplukhina[15], D. Terranova[8], D. Testa[15], C. Theiler[15], A. Thornton[5], P. Tolias[22], L. Tophøj[43], W. Treutterer[37], G.L. Trevisan[8], M. Tripsky[36], C. Tsironis[40], C. Tsui[15], O. Tudisco[44], A. Uccello[23], J. Urban[29], M. Valisa[8], P. Vallejos[22], M. Valovic[5], H. Van den Brand[19], B. Vanovac[19], S. Varoutis[33], S. Vartanian[6], J. Vega[35], G. Verdoolaege[9], K. Verhaegh[57], L. Vermare[34], N. Vianello[8,15], J. Vicente[30], E. Viezzer[37], L. Vignitchouk[22], W.A.J. Vijvers[15,19], F. Villone[17], B. Viola[44], L. Vlahos[3], I. Voitsekhovitch[5,18], P. Vondráček[29], N.M.T. Vu[6], D. Wagner[37], N. Walkden[5], N. Wang[20], T. Wauters[36], M. Weiland[37], V. Weinzettl[29], E. Westerhof[19], M. Wiesenberger[25], M. Willensdorfer[37], M. Wischmeier[37], I. Wodniak[12], E. Wolfrum[37], D. Yadykin[12], R. Zagórski[28], I. Zammuto[37], P. Zanca[8], R. Zaplotnik[32], P. Zestanakis[40], W. Zhang[9], S. Zoletnik[56], M. Zuin[8] and the ASDEX Upgrade, MAST and TCV Teams

[1] Department of Applied Physics, Aalto University, PO Box 14100, FI-00076 Aalto, Finland
[2] Aix-Marseille Université, CNRS, PIIM, F13013 Marseille, France
[3] Aristotle University of Thessaloniki, Thessaloniki, Greece
[4] Barcelona Supercomputing Center, Jordi Girona 29, 08034 Barcelona, Spain
[5] CCFE, Culham Science Centre, Abingdon, Oxon, OX14 3DB, United Kingdom
[6] CEA IRFM, F-13108 Saint Paul Lez Durance, France
[7] Department of Physics, Centre for Fusion, Space and Astrophysics, Warwick University, Coventry CV4 7AL, United Kingdom
[8] Consorzio RFX, Corso Stati Uniti 4, 35127 Padova, Italy
[9] Department of Applied Physics UG Ghent University St-Pietersnieuwstraat 41 B-9000 Ghent Belgium
[10] Department of Earth and Space Sciences, Chalmers University of Technology, SE-41296 Gothenburg, Sweden
[11] Department of Electrical and Electronic Engineering, University of Cagliari, Piazza d'Armi 09123 Cagliari, Italy
[12] Department of Physics and Astronomy, Uppsala University, SE-75120 Uppsala, Sweden
[13] Department of Physics, Durham University, Durham, DH1 3LE, United Kingdom
[14] Department of Physics, University of Strathclyde, 107 Rottenrow, Glasgow G4 0NG, United Kingdom
[15] Ecole Polytechnique Fédérale de Lausanne (EPFL), Swiss Plasma Center (SPC), CH-1015 Lausanne, Switzerland
[16] Eindhoven, University of Technology PO Box 513 NL-5600 MB Eindhoven, The Netherlands
[17] ENEA/CREATE, DIEI, Università di Cassino, Via Di Biasio 43, 03043, Cassino (FR), Italy
[18] EUROfusion PMU, Boltzmannstraße 2, 85748, Garching, Germany
[19] FOM Institute DIFFER - Dutch Institute for Fundamental Energy Research, The Netherlands
[20] Forschungszentrum Jülich GmbH, Institut für Energie- und Klimaforschung—Plasmaphysik, 52425 Jülich, Germany
[21] Foundation of Research and Technology, Crete, Greece
[22] Fusion Plasma Physics, EES, KTH, SE-10044 Stockholm, Sweden
[23] IFP-CNR, Via R. Cozzi 53, 20125 Milano, Italy
[24] Institut für Angewandte Physik, Technische Universität Wien, Wiedner Hauptstraße 8-10, 1040 Wien, Austria
[25] Institut für Ionen- und Angewandte Physik, Universität Innsbruck, Technikerstraße 25, 6020 Innsbruck, Austria
[26] Institut für Theoretische Physik, Technische Universität Graz, 8010 Graz, Austria
[27] Institute of Nuclear Techniques, Budapest University of Technology and Economics, PO Box 91, H-1521 Budapest, Hungary
[28] Institute of Plasma Physics and Laser Microfusion, Hery 23, 01-497 Warsaw, Poland
[29] Institute of Plasma Physics AS CR, Za Slovankou 1782/3, 182 00 Praha 8, Czechia
[30] Instituto de Plasmas e Fusão Nuclear, Instituto Superior Técnico, Universidade de Lisboa, Portugal
[31] ITER Organization, Route de Vinon, CS 90 046, 13067 Saint Paul Lez Durance, France
[32] Jožef Stefan Institute, Jamova 39, SI-1000 Ljubljana, Slovenia
[33] Karlsruhe Institute of Technology, PO Box 3640, D-76021 Karlsruhe, Germany
[34] Laboratoire de Physique des Plasmas, CNRS UMR7648, Ecole Polytechnique, 91128 Palaiseau, France
[35] Laboratorio Nacional de Fusión, CIEMAT, Madrid, Spain
[36] Laboratory for Plasma Physics Koninklijke Militaire School—Ecole Royale Militaire Renaissancelaan 30 Avenue de la Renaissance B-1000, Brussels, Belgium
[37] Max-Planck-Institut für Plasmaphysik, D-85748 Garching, Germany

[38] Max-Planck-Institut für Plasmaphysik, Teilinstitut Greifswald, D-17491 Greifswald, Germany
[39] National Institute for Laser, Plasma and Radiation Physics, PO Box MG-36, Bucharest, Romania
[40] National Technical University of Athens, Athens, Greece
[41] Politecnico di Torino, Dipartimento di Elettronica e Telecomunicazioni (DET), Torino, Italy
[42] Rudolf Peierls Centre for Theoretical Physics, University of Oxford, Oxford, UK Culham Centre for Fusion Energy, Abingdon, United Kingdom
[43] Department of Physics, Technical University of Denmark, Bldg 309, DK-2800 Kgs Lyngby, Denmark
[44] Unità Tecnica Fusione—ENEA C. R. Frascati—via E. Fermi 45, 00044 Frascati (Roma), Italy
[45] Universidad de Sevilla. C/ S. Fernando, 4, C.P. 41004-Sevilla, Spain
[46] Université de Lorraine, Institut Jean Lamour, Vandoeuvre-lés-Nancy, 54000 Nancy, France
[47] Université Grenoble Alpes, LCIS, F26902 Valence, France
[48] University College Cork (UCC), Ireland
[49] University Milano-Bicocca, Piazza della Scienza 3, 20126 Milano, Italy
[50] Department of Physics, University of Helsinki, PO Box 64, FI-00014 University of Helsinki, Finland
[51] University of Napoli 'Federico II', Consorzio CREATE, Via Claudio 21, 80125 Napoli, Italy
[52] University of Napoli Parthenope, Consorzio CREATE, Via Claudio 21, 80125 Napoli, Italy
[53] University of Rome Tor Vergata, Via del Politecnico 1, 00133 Rome, Italy
[54] University of Split, Faculty of Electrical Engineering, Mechanical Engineering and Naval Architecture, R. Boskovica 32, 21 000 Split, Croatia
[55] VTT Technical Research Centre of Finland, PO Box 1000, FI-02044 VTT, Finland
[56] Wigner Research Centre for Physics, PO Box 49, H—1525 Budapest, Hungary
[57] York Plasma Institute, Department of Physics, University of York, Heslington, York, YO10 5DD, United Kingdom
[58] ICREA, Pg. Lluís Companys 23, 08010 Barcelona, Spain

E-mail: Hendrik.Meyer@ccfe.ac.uk

Received 18 November 2016, revised 22 December 2016
Accepted for publication 25 January 2017
Published 28 June 2017

Abstract

Integrating the plasma core performance with an edge and scrape-off layer (SOL) that leads to tolerable heat and particle loads on the wall is a major challenge. The new European medium size tokamak task force (EU-MST) coordinates research on ASDEX Upgrade (AUG), MAST and TCV. This multi-machine approach within EU-MST, covering a wide parameter range, is instrumental to progress in the field, as ITER and DEMO core/pedestal and SOL parameters are not achievable simultaneously in present day devices. A two prong approach is adopted. On the one hand, scenarios with tolerable transient heat and particle loads, including active edge localised mode (ELM) control are developed. On the other hand, divertor solutions including advanced magnetic configurations are studied. Considerable progress has been made on both approaches, in particular in the fields of: ELM control with resonant magnetic perturbations (RMP), small ELM regimes, detachment onset and control, as well as filamentary scrape-off-layer transport. For example full ELM suppression has now been achieved on AUG at low collisionality with $n = 2$ RMP maintaining good confinement $H_{\mathrm{H(98,y2)}} \approx 0.95$. Advances have been made with respect to detachment onset and control. Studies in advanced divertor configurations (Snowflake, Super-X and X-point target divertor) shed new light on SOL physics. Cross field filamentary transport has been characterised in a wide parameter regime on AUG, MAST and TCV progressing the theoretical and experimental understanding crucial for predicting first wall loads in ITER and DEMO. Conditions in the SOL also play a crucial role for ELM stability and access to small ELM regimes.

Keywords: edge localised modes, divertor, heat loads, ASDEX upgrade, MAST, TCV, alternative divertor concepts

(Some figures may appear in colour only in the online journal)

1. Introduction

One of the key challenges in the realisation of a magnetic confinement fusion power plant is to integrate the high-confinement core with the edge of the plasma, such that acceptable wall conditions are obtained whilst maintaining high performance. In particular the periodic transient heat loads due to edge localised modes (ELM) [1, 2] in the otherwise promising high confinement mode will not be tolerable in ITER and DEMO [3]. Cyclic thermo-mechanical loads may limit the number and size of ELMs to much smaller values than design criteria to prevent melt damage, especially in DEMO. For the achievement of physics understanding of the plasma edge and the ability to extrapolate the findings to future devices, a wide parameter range needs to be investigated. This is a task ideally suited to the new European task force on medium sized tokamaks (EU-MST) that has combined research on three key, complementary devices ASDEX Upgrade (AUG), TCV and MAST since 2014.

Research under the EU-MST task force tackles the edge challenge from two sides. On the one hand, plasma regimes reducing the transient heat loads whilst trying to maintain high confinement are developed with active ELM control techniques (section 2) and natural small ELM scenarios (section 3). On the other hand, divertor solutions with detachment control (section 4) and advanced magnetic configurations (section 5) are studied. In this paper we will give an overview of the progress made in the last two years in these two research fields within EU-MST supported by the domestic programs. In addition, we will discuss the enhanced filamentary radial transport in the scrape-off layer (SOL) becoming more important as transient heat loads on the divertor targets are reduced (section 6). Studies have been performed in D, H and He as the main discharge species to assess the feasibility of the methods for the non-nuclear phase in ITER.

2. Reducing the ELM size with actuators

Approximations to the ITER baseline scenario on AUG ($3 \leqslant q_{95} \leqslant 3.6$, $n/n_G = 0.85$, $\beta_N = 1.8$) show that the low q_{95} and high triangularity lead to low frequency ELMs with exceptionally large energy loss of up to 45% of the pedestal energy on AUG [5] (see figure 1). Whilst sometimes these large energy losses can be attributed to multiple clearly distinguishable crash events sometimes called compound ELMs, here also long ELMs with crash times of the order of up to 8 ms are observed (see below) that show some small substructure in the signal for the divertor current. The relative ELM energy losses in the AUG variant of the ITER base-line scenario lie well above the scaling from Loarte *et al* [4]. Gas fuelling can reduce the ELM size, but will lead to a degradation of the confinement due to the erosion of pedestal pressure, as also seen on JET [6]. A likely reason for this reduction in p_{ped} is the presence of a high density front at the high field side [7], which leads to an outward shift of the density pedestal, in turn leading to a reduction of the peeling-ballooning stability. The scenario has also proven resilient to active ELM mitigation techniques such as pellet triggering or application

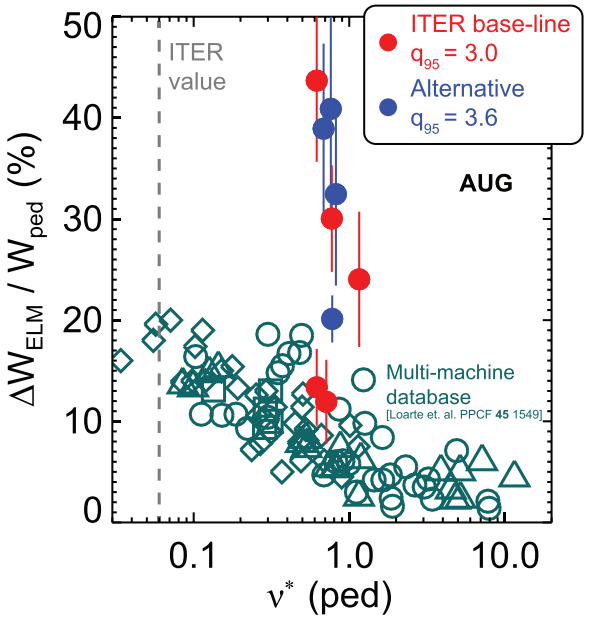

Figure 1. Relative ELM energy loss of the ITER base-line scenario at $q_{95} = 3$ (red) and its $q_{95} = 3.6$ (blue) variant in comparison to the data (open symbols) showing the ν^* scaling from a multi-machine database [4]. The different open symbols represent different devices.

of resonant magnetic perturbations (RMP). Application of RMPs has led to a clear, though small density pump-out, but not an increase of ELM frequency or reduction in ELM energy loss. Interestingly, a slight vertical upshift approaching a double null configuration or reduction in divertor pumping gives access to a small ELM regime, not unlike the type-II ELM regime (see section 3) [5, 8]. Assessing the performance of the ITER base-line scenario and its variant in high purity He plasmas ($(n_{He}/(n_{He} + n_H + n_D) \gtrsim 80\%$) shows a similar ELM behaviour with larger ELMs $\Delta W_{ELM} \approx 50$ kJ ($\Delta W_{ELM}/W_{pl} \approx 10\%$) at lower neutral density and small ELMs at high neutral density in the divertor. The new neutral beam injection on TCV has enabled studies of these high density regimes on TCV, and scenario development has been started.

For single events, the peak parallel ELM energy fluence, $\epsilon_{\parallel}(s) = \varepsilon_{div}/\sin\alpha_{div}$ with $\varepsilon_{div} = \int q(s,t)\mathrm{d}t$ the energy fluence to the divertor target (q heat flux, s spatial target coordinate, α_{div} field line angle on the target), of natural type-I ELMs on ASDEX Upgrade and JET never exceeds a value proportional to the pedestal top pressure, p_e^{ped}, times the geometric minor radius, a [9]. This data set has now been extended to MAST and discharges with active ELM control, and will be extended to TCV in the future.

In figure 2 the comparison of the measured $\max(\epsilon_{\parallel})$ to a simple ad hoc model of a toroidally symmetric reconnected flux tube

$$\max(\epsilon_{\parallel}{}^{\mathrm{model}}) = \Delta_{\mathrm{eqil.}} 2\pi a \sqrt{\frac{1+\kappa^2}{2}} \frac{3}{2} p_e^{\mathrm{ped}} \frac{B_t}{B_p} \approx 6\pi\, p_e^{\mathrm{ped}} R_{\mathrm{geo}}$$

is shown (κ: elongation, q_{cyl}: cylindrical safety factor, $R_{geo.}$: geometric major radius) [9, 10], where $1.8 \leqslant \Delta_{eqil.} \leqslant 2.3$ accounts for the difference of the flux tube volume between a simplified

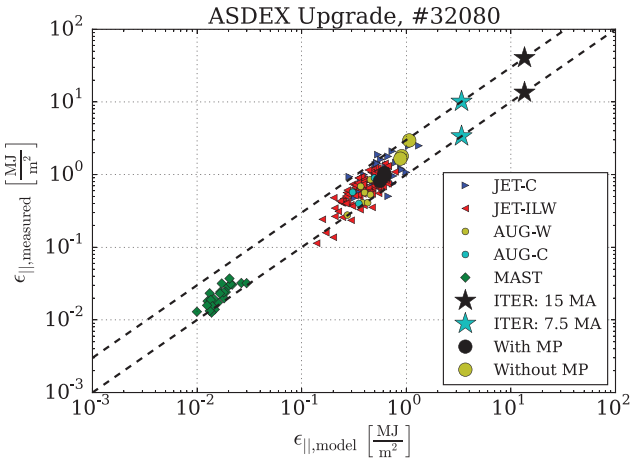

Figure 2. Measured type-I peak ELM energy fluence against model prediction for a multi-machine database including AUG, JET and MAST [10]. Reproduced with permission from [10].

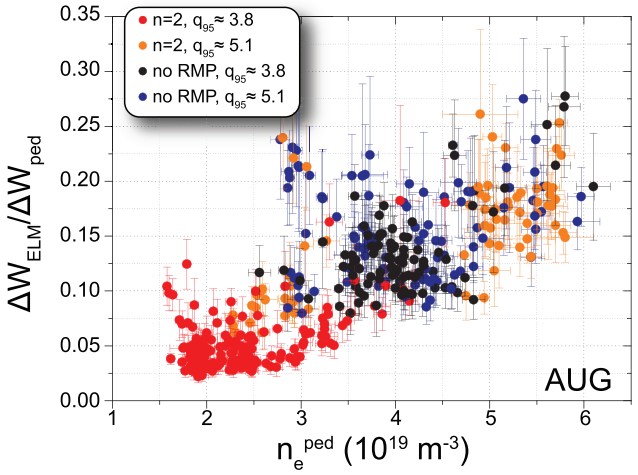

Figure 3. Normalised ELM energy loss as a function of electron density at the pedestal top before the ELM, with and without RMP and two different edge safety factors. Reproduced from [19]. © IOP Publishing Ltd. All rights reserved.

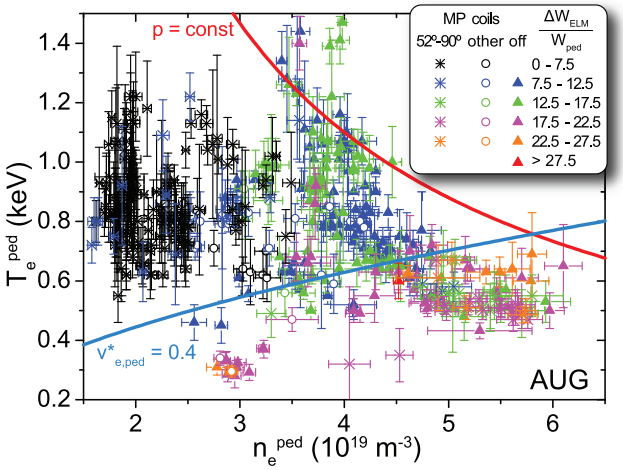

Figure 4. Operating space in temperature and density for discharges with and without RMP for different ELM energy losses. Reproduced from [18]. © 2017 Max-Planck-Institut für Plasmaphysik.

approximation and the accurate value derived from the equilibrium reconstruction. Over two orders of magnitude the data is within a factor of three of this simple prediction, which gives a lower bound to the data. The data set includes data from the inner and outer divertor of AUG, as well as shots with ELM control using pellets and vertical kicks in the case of JET and RMPs in case of AUG. The data presented in figure 2 are favourable for ITER, suggesting that even unmitigated type I ELMs in the baseline $Q_{DT} = 10$ scenario at $I_p = 15$ MA may lead to target energy densities which are close to, or only slightly exceed (by factors of 2–3) the currently specified ELM energy density limit ($\varepsilon_{tar} = 0.5$MJ m^{-2} [11]). This is a significant gain compared with the mitigation factors (>20) which were previously thought to be imposed by this limit. The limit was, however, established according to specifications which must now be modified in the light of improved studies of tungsten material response to high transient numbers [3] and refinements in the ITER divertor target design and associated calculations of energy loading. In particular, the presence of target monoblock surface shaping, the inevitable gaps between the monoblocks and the requirement to operate below recrystallization temperature will all lower the previously specified allowed energy density [12]. Work is ongoing at the ITER Organization in collaboration with the EUROFusion Programme (as well as other ITER Partners) to establish a new material limit.

In figure 2 data of an AUG discharge with RMPs at low collisionality are shown as well. As for the cases of ELM control in JET the RMP data fits into the overall trend. In detail, the application of RMPs increases the ELM frequency on AUG, but also reduces the pedestal pressure due to the density pump out. It should be noted that this trend is only true for cases where the ELMs are still of type I. It is unclear if ELM control/mitigation techniques for type-I ELMs will be able to move the ELM heat loads from the upper boundary to or below the lower boundary whilst maintaining the pedestal pressure in a robust way. In any case these data suggest that even mitigated type-I ELMs may not be acceptable for the $Q_{DT} = 10$ scenario in ITER and are most likely unacceptable for DEMO.

In certain ELM cycles on MAST the density lost due to the application of RMPs could be replaced by gas fuelling whilst maintaining a reduced ELM energy loss [13]. Similar studies have been performed on AUG using pellets fuelling under ITER-like conditions [14]. In these experiments the full density pedestal could be recovered. To refuel a density pump-out of 30% the fuelling rate had to be increased by a factor of two. However, it was not possible to fully recover the loss of confinement as the increase of the density lead to a decrease of temperature and the pedestal pressure could only be partly restored. As increased gas fuelling also affects ELM stability [7, 15, 16], degrades confinement [6, 7] and can be used to control the ELM frequency [17], the increased recycling due to the increased fuelling rate may also play a role in the loss of confinement. Pellet refuelling during RMPs did not trigger further ELMs and a mitigation of the ELM energy loss, albeit at a compromised level, was maintained [14]. Within the scatter of the data the average peak heat load $q_{peak} \approx 4$ MW m^{-2} during the RMP phase with and without pellets did not change. Comparison to the pre RMP phase,

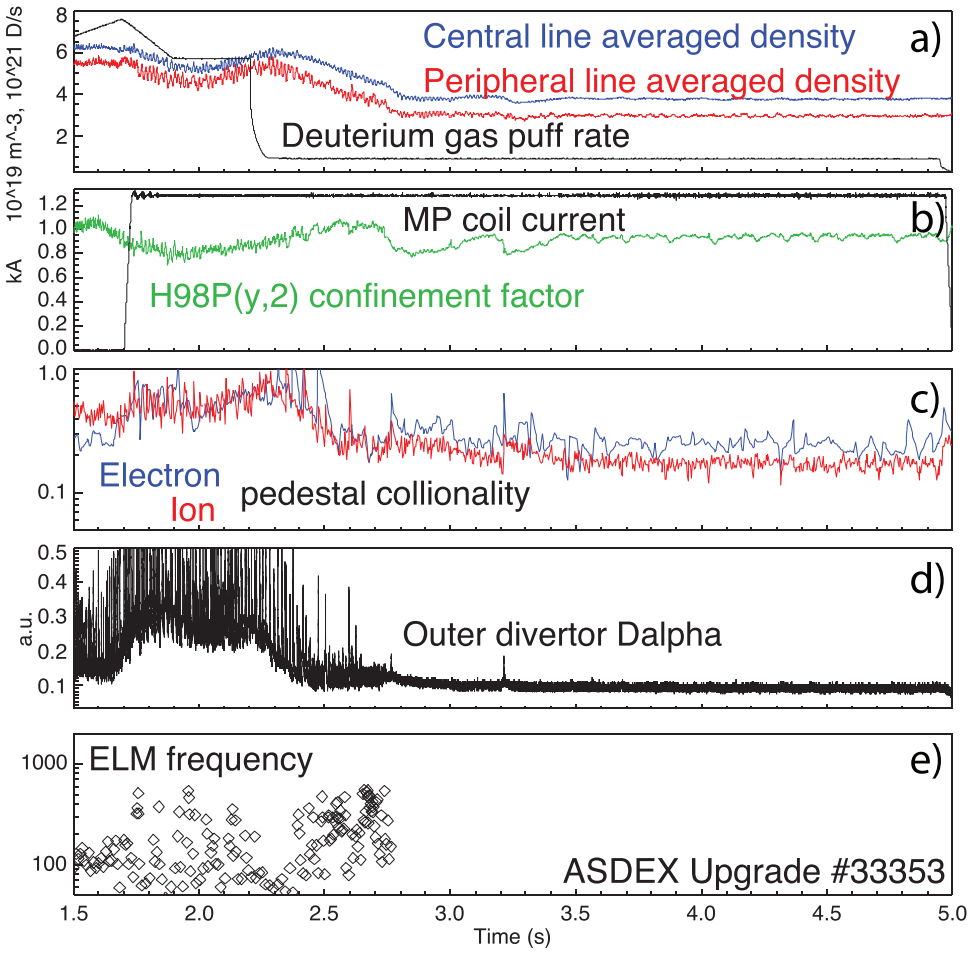

Figure 5. Typical time traces for a low collisionality discharge on AUG where ELM suppression was achieved. Reproduced from [18]. © 2017 Max-Planck-Institut für Plasmaphysik.

however, showed that the application of RMPs in this case only reduced q_{peak} by a factor of two. This is consistent with the reduction in average normalised ELM energy loss as inferred from the inverse frequency behaviour, implicitly assuming that the energy loss rate by ELMs is the same as the long term energy loss rate.

The interplay between increased particle transport (e.g. density pump-out) and the efficiency of ELM control at low collisionality is a key question in extrapolating to future devices that will have low collisionality at high Greenwald fraction [18]. Analysis of the AUG data base of low collisionality discharges using $n = 2$ RMP to affect the ELMs has shown that the ELM energy loss correlates best with the edge density (see figure 3) and less well with pedestal collisionality [18, 19]. However, a threshold of $\nu^{*}_{\mathrm{ped}} \lesssim 0.4$ has been found, above which ELMs are not affected (figure 4). At the lowest edge density the loss of stored energy during an ELM can be reduced by 85%, but as can be seen from figure 4 not at an isobar corresponding to type I ELMy H-mode [13, 19]. At this parameter regime the low density branch of type III ELMs (also called type IV) is found on DIII-D [20] and MAST [13]. On DIII-D and MAST type-IV regimes can also be accessed without RMPs. Experiments with coil waveforms optimised to achieve a fast switch-off, proved that on AUG it is not only the reduction in density that gives access to the small ELMs.

More recently, ELM suppression was observed at low collisionality $\nu^{\star}_{\mathrm{e,ped}} \leqslant 0.25$ on AUG (see figure 5) [18] in a higher triangularity $\delta_{u/l} = 0.23/0.43$ DIII-D/AUG identity shape. The experiments on DIII-D revealed the crucial role of the triangularity for accessing full ELM suppression motivating the shape change on AUG. The suppression phase, starting at $t = 2.75$ s, is initiated by a reduction in gas fuelling leading to a drop in density between $t = 2.30$–2.75 s and is accompanied by a further, faster drop in density. Consequently, this leads to a drop in confinement by 25% with respect to the mitigated phase. However, the confinement soon recovers, reaching $H_{\mathrm{H(98y,2)}} \lesssim 0.95$ stably from $t = 3.45$ s onwards. This is comparable to the ELM mitigation phase ($t = 2.5$–2.75 s), which in this shape has considerably higher confinement than in the low $\delta_{u/l} = 0.1/0.43$ shape.

A key part of the RMP experiments under EU-MST was directed towards the understanding of the plasma response. Comparing the experimental data with plasma response calculations using the resistive MHD code MARS-F [21–23] confirmed the findings from MAST that the edge kink response needs to be maximised to affect the ELMs and is in good agreement with differential phase scans performed on AUG and MAST. The optimal phase angle for the applied perturbation depends roughly linearly on q_{95} [23], but also on β [24]. An analytical model based on dedicated scans of MARS-F starting

from an example equilibrium has been developed to predict the phase angle prior to experiments to within ±20° [24] by optimising the plasma response with respect to the displacement close to the X-point (kink response) and the perturbation at the outermost resonance. Measurements of the 3D perturbation of the plasma around the mid-plane using several diagnostics by rotating the perturbation field at constant phase angle between the upper and lower coils show good agreement with plasma response modelling using the 3D equilibrium code VMEC as well as MARS-F [25]. The magnetic perturbation was found to be amplified by the plasma and to be primarily non-resonant $|m| > |nq|$, whilst the displacement is dominated by resonant components $|m| = |nq|$ as predicted by the codes [25]. Resonant modes arise via toroidal and elongation mode coupling [22]. The plasma response calculations have now been extended to the non-ideal MHD code JOREK [26], showing good agreement with VMEC and MARS-F calculations, together with qualitative agreement of the observed change in magnetic mode spectrum during the ELM [27] as well as the filamentary dynamics measured with ECE imaging [28].

ELM energy loss mitigation was also achieved in He discharges at low collisionality. The phase angle of the applied perturbation is similar to that measured in D. Small differences may be explained by the lower β achieved in He. This shows that it should be possible to transfer the experience gained during a potential non-activation He phase on ITER to D and DT. The ELMs are affected by the RMP in He at similar density as in D. However, the lower pedestal temperature in He leads to a much higher collisionality, at which in D ELM control with RMPs is not possible on AUG. This suggests that the collisionality is not the only factor determining the effect of RMPs. It should be noted, though, that ELM mitigation can be achieved on MAST with almost all edge collisionalities [13]. For the higher collisionality ITER base-line scenarios pump-out as in D could be observed, but ELMs became larger at the lower density.

The physics of ELM energy loss mitigation at low and high collisionality on AUG is different. At high collisionality the RMP spectrum or alignment does not play a role [29]. Experiments at different plasma current and heating power showed that these mitigated ELMs are also likely a different ELM regime [30]. In contrast to the low collisionality regime, however, this regime also persists without magnetic perturbation (see section 3).

The potential for ELM control with pellets in metal walled devices is greatly reduced due to a dead time after the previous ELM [31]. Injection of N recovers the trigger potential. Analysis of the inter ELM pedestal evolution on AUG shows that with and without N seeding ELMs can be triggered after the fast density recovery phase [32]. This may be related to the existence of long and short ELMs in all-metal devices [33]. A long ELM, having an extra 2nd phase expelling filaments into the SOL [33], will degrade the pedestal more than a short ELM. Comparisons on AUG, JET and TCV of ELMs with and without N seeding seem to point at the crucial role of the SOL temperature [34] for the existence of the 2nd phase. It should be noted that the estimated $max(\epsilon_{\parallel})$ of N seeded ELMs is higher than of unseeded ELMs due to the faster deposition of the energy onto the target and the smaller wetted area. However, N also leads to earlier detachment of the divertor (see section 4).

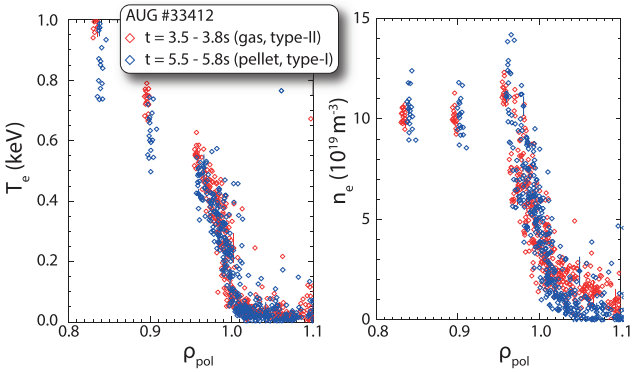

Figure 6. Comparison of the electron temperature (left) and density (right) profiles in a gas fuelled phase (red) and dominantly pellet fuelled phase (blue) from Thomson scattering at otherwise constant discharge parameters.

3. Small ELM regimes

Not only type-I ELMs are affected by the SOL; the onset of type-II ELMs is also likely related to the SOL conditions. Comparison of the filamentary structure of type-II ELMs between AUG and MAST suggested the origin of the type-II ELM filaments to be at the foot of the pedestal [35]. Type-II and type-I ELMs can coexist, giving further evidence for their different origin.

Recently, the proximity of the ITER base-line scenario on AUG to small (type-II like) ELMs was discovered [5]. Replacing the gas fuelling in these discharges with pellet fuelling from the high field side ($l = 1.9$ mm, $f = 35$ Hz, $v = 552$ m s^{-1}, $\Gamma_{\mathrm{pellet}} = 1.3 \times 10^{22}$ D s^{-1}) reduced the SOL density, as can be seen in figure 6 (right). The pedestal pressure was kept constant, and the gradients of temperature and density are also the same within the error bars in both phases. However, the pellet fuelled phase has type-I ELMs, whilst the gas fuelled phase exhibits small ELMs. The pellets penetrate roughly to $\rho \approx 0.8$ and fuel the plasma about three times more efficiently than the gas puff ($\Gamma_{\mathrm{gas}} = 3.3 \times 10^{22}$ D s^{-1}).

Experiments using $n = 2$ magnetic perturbations (MP) during strong fuelling ramps revealed the importance of the increasing intermittent transport for the occurence of small ELMs [30]. Discharges with three different plasma currents ($I_{\mathrm{p}} = 0.6$, 0.8 and 1.0 MA) and two different heating levels ($P_{\mathrm{heat}} = 6.3$ and 8.7 MW) were performed in order to try to separate collisionality from density. Here, type-I ELMs and small filaments coexist at lower fuelling levels and are fully replaced by small ELMs as the fuelling is increased. At the highest fuelling levels small ELMs persist even without MP. Hence, the MP is not necessary for the small ELMs to occur. In figure 7 the electron density (left) and temperature (right) for three time points for the $I_{\mathrm{p}} = 0.6$ MA case are shown. With increasing fuelling n_e^{sep} and n_e^{ped} rise. With increasing $\nu^{\star}$ the filaments become larger and form the n_{e} shoulder in the SOL. The larger filaments occur together with a wider near SOL mid-plane T_{e} decay length, the pedestal becomes wider and its gradient is shallower, due to the lower $T_{\mathrm{e}}^{\mathrm{ped}}$. The pedestal is (filamentary) transport limited and not peeling–ballooning limited as for type-I ELMs. The perturbation of the equilibrium by the MP leads to lobe structures,

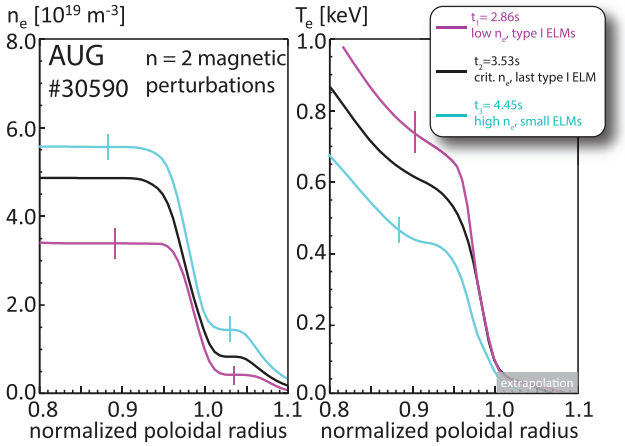

Figure 7. Comparison of the electron density (left) and temperature (right) profiles for three time points during a gas scan with the application of $n = 2$ magnetic perturbations. Reproduced with permission from [30].

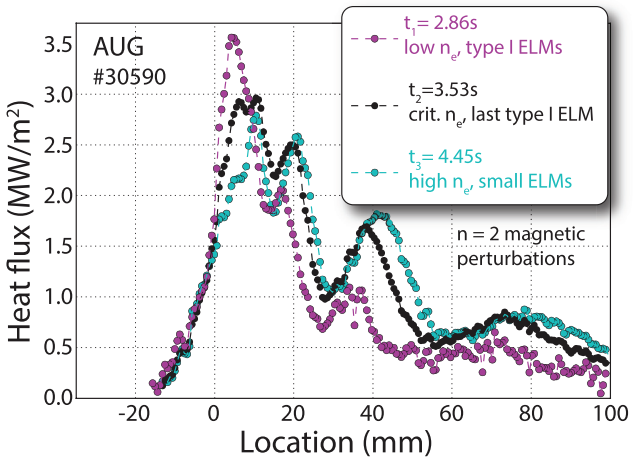

Figure 8. Comparison of the heat flux profiles at the outer divertor target for three time points during a gas scan with the application of $n = 2$ magnetic perturbations. Reproduced with permission from [30].

clearly observable in the heat flux profile (see figure 8). As the density rises with increasing fuelling the cross-field transport in the SOL is enhanced and the SOL becomes wider (see section 6). The application of MPs forms homoclinic tangles [36] that are filled by this enhanced cross-field transport, leading to a population of lobes further away from the unperturbed separatrix, and finally to the onset of detachment. The presence of the MP may influence the density at which the general cross field transport changes.

These results, as well as the N seeding experiments, point towards the importance of the SOL for the onset of small ELM regimes and the ELM stability as such. The SOL at high power high density discharges on AUG is closer to ITER/DEMO parameters than the SOL in low collisionality plasmas. To date it is unclear if the transport leading to the small ELM regime can be achieved at low collisionality and high density at the same time. Trying to decrease $\nu^{\star}$ in small ELM regimes by stronger heating usually leads to an increased density with a clamped pedestal temperature. The pedestal pressure achieved in these regimes is close to that of type-I ELMy H-mode.

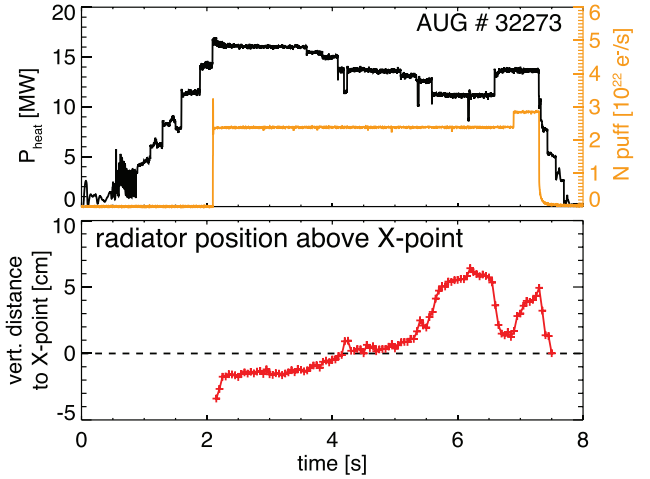

Figure 9. Vertical position of the radiator relative to the X-point in AUG #32273 with the modulation of heating power and N seeding. Reproduced from [83]. CC BY-NC-ND 4.0.

The ELM energy loss is also reduced close to the density limit whilst maintaining high confinement. This phase has not yet been extended into a stable scenario, but the four phases of the H-mode density limit identified on AUG [37] have now also been observed on TCV despite the different divertor geometry.

4. Buffering the divertor

Partial detachment of the divertor is a key part of the integrated solution and has long been studied in conventional divertor configurations. Controlling the divertor temperature—estimated from the thermal currents flowing in the SOL—using nitrogen influx as an actuator is well established on AUG [38]. This method may not be suitable for next step devices as it requires isolated tiles in a neutron environment, and other observers may be needed for detachment control. Recently the position of a poloidally localised radiator close to the X-point, as measured by bolometry, has been identified as such a possible observer [39]. The time evolution of the vertical position of this X-point radiator for a discharge with varying heating power and N seeding is shown in figure 9 at high $P/R \lesssim 10$ MW m^{-1}. With a reduction of heating power, this radiator moves further inside the confined region—and, with an increase of the heating power, the equilibration point of the radiator moves closer to the X-point. The increase of the N seeding levels leads again to an inward movement. If the radiator moves too far inside the confined region, a disruption is triggered. The stability of the poloidal asymmetry is likely facilitated by the long connection length around the X-point. This is also observed in advanced divertor configurations (see section 5).

Furthermore, different seeding gases (N, Ne, Ar, Kr) were used to control radiation in different areas of the plasma. Detached operation has been achieved with the highest $P/R \leqslant 15$ MW m^{-1} at Greenwald fractions of $n_e/n_G \approx 90\%$ and high $H_{H(98,y2)} \lesssim 0.95$, though at high radiation and density $H_{H(98,y2)}$ may not be the appropriate measure. A key point in

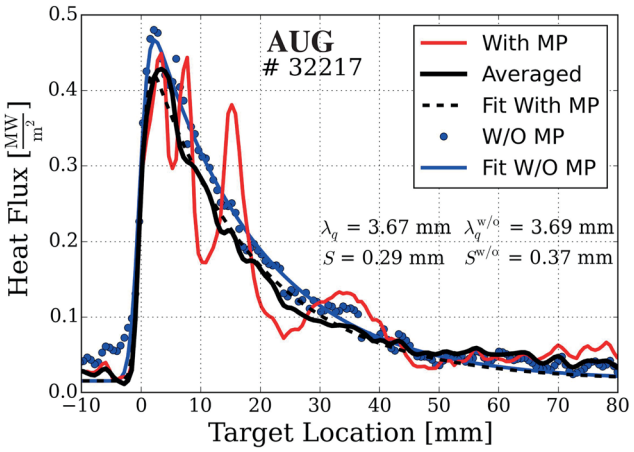

Figure 10. L-mode heat flux profile on the outer divertor with MP (red) and without (blue). The toroidally averaged profile in the presence of MP (black) leads to the same distribution as the axisymmetric one.

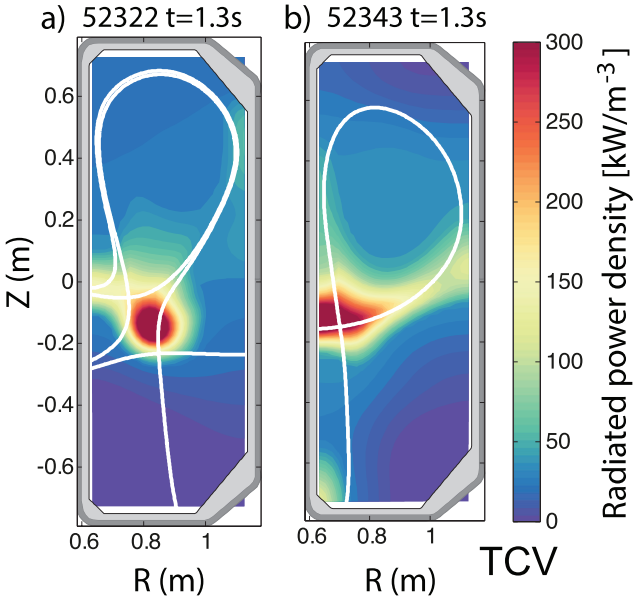

Figure 11. Comparison of the tomographically inverted radiation in (*a*) a LFS SF$^-$ and (*b*) a conventional divertor configuration at similar discharge conditions and seeding levels. Reproduced with permission from [84].

understanding this physics is the accurate modelling of the fuelling sources and impurity transport in the SOL. Using the SOLPS5.0 code the high field side high density region on AUG and the effect N seeding has on this front has been modelled [40]. Adapted diffusive and additional convective radial transport coefficients now reconcile the modeled deuterium compression ratio, divertor neutral density, neutral radiation levels and deuterium fueling rates with experimental measurements. The onset of strong volume recombination in the simulations now allows removal of the previously necessary increase of perpendicular transport in the inner divertor from the simulations.

The application of 3D fields for ELM control will also impact on the divertor heat load, by breaking the toroidal symmetry leading to regions of increased heat load far from the strike point. Clear lobe structures are seen in the heat flux pattern at low and high collisionality on AUG [41] and MAST [42, 43]. Such structures have also been observed on other devices with the application of MPs such as DIII-D [44], EAST [45], JET [42, 46] and NSTX [47] and have been compared usually to vacuum calculations which generally represent the pattern well in L-mode. Using slowly rotating fields on AUG the full toroidal variation of these patterns has been measured with IR imaging for the first time in L- and H-mode discharges with $n = 1, 2, 3$ RMPs [41]. In L-mode the heat flux profile averaged over a rotation of the perturbation by $2\pi/n$ will recover the unperturbed heat load profile (see figure 10), showing that the cross field transport in L-mode is much higher than a potential effect due to the perturbation itself. Such outward transport could come from a stochastic layer [48]. A new method to measure this layer using ECRH heat pulses in comparison with EMC3 modelling using an ad hoc screening model has been employed on AUG [49]. The analysis of L-mode discharges also showed no significant difference of the temporal behaviour of the heat pulse with and without RMPs. It should be noted that the application of RMPs can also lead to localised fast-ion losses [50, 51] that may cause localised heat loads to the first wall [52].

5. Advanced divertors

The work on detachment has been extended to the advanced divertor configurations studied experimentally on TCV [53, 54] and theoretically for MAST Upgrade geometry [55, 56]. These configurations aim to reduce the heat load of the target by geometrical means such as flux expansion as well as by increasing perpendicular transport and volumetric processes. EMC3-Eirene calculations of various TCV snowflake configurations, for example, predicted that a snowflake configuration with an additional X-point in the low field side SOL (SF-) would not only reduce the heat loads on the outer target, but that impurity seeding should create a highly radiating zone trapped between the two X-points with a large volume [57].

This predicted trapped radiation zone has now been observed experimentally (see figure 11). With respect to power balancing, however, fluid modelling is not able to reproduce the power distribution between the different strike points correctly when the secondary strike points are not connected to the SOL (SF$^+$). In particular, more power than the modelling suggests arrives at the passive strike points in these snowflake configurations [58], and double peaked profiles are also observed [59]. Enhanced $E \times B$ drifts in the SF configuration could explain the power distribution. The $E \times B$ drifts are predicted to increase with density, increase with low distance between the X-points and reverse sign with B_t. All these predictions are in qualitative agreement with the measurements [58].

The dependence of the onset and the evolution of detachment on poloidal flux expansion (incl. strike point flaring 'X-divertor') f_x, major radius R_{OSP} of the outer strike point (toroidal flux expansion,'Super-X'), the appearance of a 2nd X-point close to the target ('X-point target divertor') at

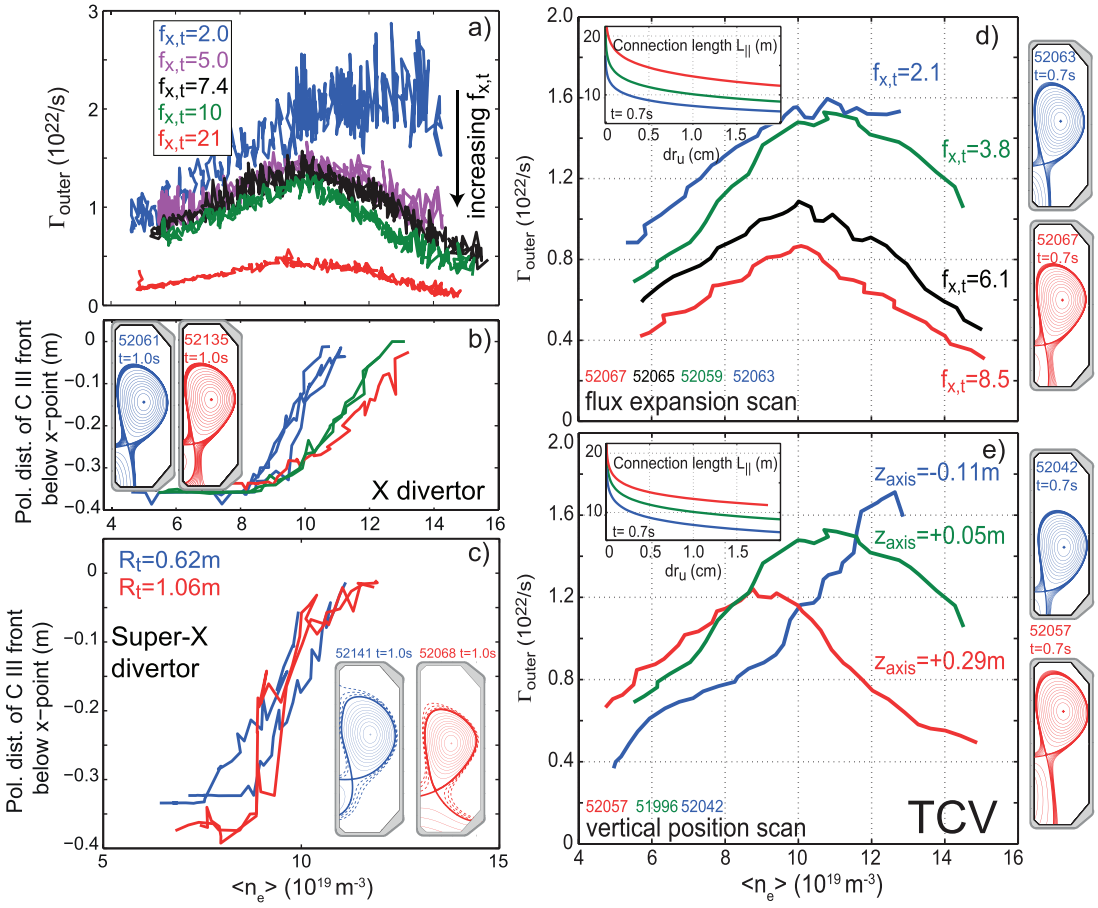

Figure 12. Measures of detachment as a function of line averaged density for ((*a*) and (*b*)) different flux expansion in the X-divertor, (*c*) Super-X divertor, (*d*) different flux expansion in the conventional divertor and (*e*) different vertical positions at constant flux expansion at the strike point. As a measure of detachment in ((*a*), (*d*) and (*e*)) the total ion flux to the outer divertor is used and in ((*b*) and (*c*)) the poloidal distance of the C^{2+} radiation front below the X-point is used. (*a*) Reproduced from [53]. CC BY 3.0. (*b*)–(*e*) Reproduced with permission from [84].

a particular $\rho_\psi = \sqrt{(\psi - \psi_0)/(\psi_a - \psi_0)}$ ($\psi_{0,a}$ poloidal flux at the separatix (a) and magnetic axis (0)) and vertical plasma height ($L\|$) have been studied in Ohmic discharges on TCV in reversed B_t/I_p [53, 54]. Here, the ion ∇B drift was away from the primary X-point, to avoid H-mode transitions. Density ramps were performed in a total of 17 configurations changing $f_x = 2$–21, $R_{OSP} = 0.62 - 1.06$ m, $\rho_\psi = 1.012,\ 1.036$ and $Z_{axis} = -0.11$ to $+0.29$ m. A change in the detachment onset has only been observed with a vertical shift of the plasma (figure 12(e)), where a longer outer divertor leg leads to a roll-over in the ion saturation current at lower density. Changes of the poloidal and toroidal flux expansion lead to a roll-over of the total ion flux at similar densities, as can be seen from figures 12(a),(b) and (d) and 12(c) respectively. At higher f_x the relative drop in particle flux seems more pronounced (figure 12(a) and (d)), which is consistent with recombination measurements performed using a new divertor spectrometer [60]. In addition, for higher values of f_x the cold plasma region tends to stay more localized to the target during an increase in core density, as indicated by C^{2+} radiation front measurements [61] and recombination measurements. Deviations of the R_{OSP} dependence from the standard 2 point model have been observed. The heat flux is reduced as expected, but the density decreases rather than increases, leading to a higher temperature at the target than predicted. The detachment onset is not affected by R_{OSP}, contradicting expectations (figure 12(c)). Hence, there is no consistent dependence on the total flux expansion. SOLPS5.0 modelling of the novel divertor currently being built for MAST Upgrade—comparing a conventional configuration to three Super-X configurations—showed, however, that the real advantage of the Super-X configuration only manifests itself with sufficient divertor closure [56], although in all Super-X configurations the heat load in comparison to the conventional divertor is reduced. It should be noted that not only the change in R_{OSP}, but also the relative change in B_t due to the tight aspect ratio configuration in these configurations, are much larger than on TCV. The progression of C^{2+} radiation front towards the core is slowed down considerably in the 'X-point target divertor' like configurations, due to the presence of the secondary X-point, similarly to what is seen in a conventional divertor around the primary X-point.

6. First wall loads

The heat and particle loads in the narrow region around the strike points are the most severe in future devices, but as the density is increased in present day devices a density shoulder forms far out into the SOL [62]. This broader SOL could be

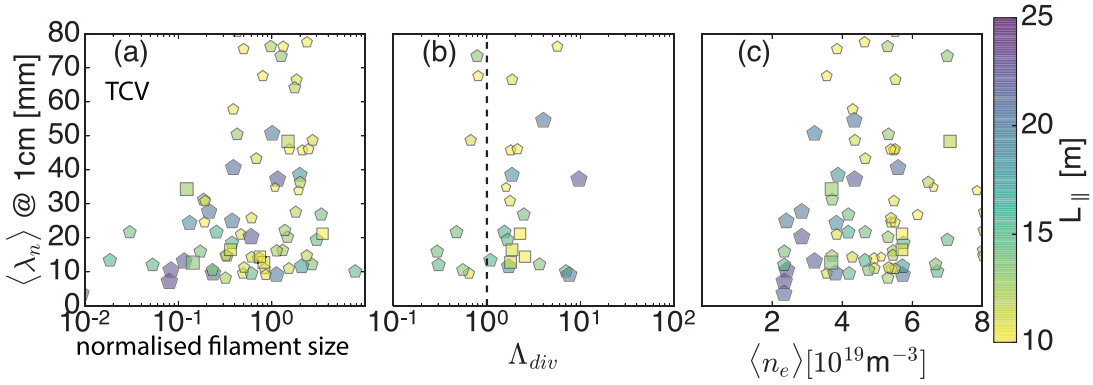

Figure 13. Density e-folding length as a function of (*a*) normalised perpendicular filament size, (*b*) effective collisionality in the divertor and average density on TCV evaluated at 1 cm outside the separatrix (⬠ DN, □ LSN). Reproduced with permission from [70].

of concern for future devices, in particular if the ion energy is above the sputtering threshold, leading to increased heat loads and impurity influx. This transport is dominantly driven by strong intermittency (filaments). The filament properties and their relation to the density shoulder formation have been investigated in detail in L-mode on AUG [63–65], MAST [66–69] and TCV [70], as well as inter-ELM H-mode phases on AUG [63, 65, 71]. The ion temperature in the filaments in the L-mode SOL could be measured using a retarding field energy analyser on AUG [65] and MAST [68, 72]. At low density $T_i/T_e \gtrsim 3$–4 in the far SOL, whilst at higher density $T_i/T_e \sim 1$.

Multi-machine L-mode data from AUG and JET in various conditions show a clear transition in filament behaviour as the effective collisionality, $\Lambda = \frac{L_\parallel \nu_{ei}}{c_s}\frac{\Omega_i}{\Omega_e}$ (c_s: sound speed, Ω cyclotron frequency) in the divertor is increased above $\Lambda_{\mathrm{div}} > 1$ [64]. The filament motion seems in broad agreement with 2D modelling [73] using cold ions [65]. The inter ELM H-mode data show that Λ_{div} may only be a necessary but not sufficient condition for the shoulder formation [63]. Matching Λ_{div} using high D fuelling and high D fuelling plus N seeding at various densities showed that the shoulder only formed at high Λ_{div} with N seeding when also sufficient D fuelling was applied. This suggests that the presence of neutrals may also be important for the shoulder formation. This is further evidenced by the filament properties measured on TCV in L-mode (see figure 13) [70]. These experiments focussed on the connection length $L_\parallel$ dependence (colors), which can be varied in TCV independently of q_{95} by moving the plasma up and down and changing the flux expansion. λ_n depends only weakly on $L_\parallel$. The strongest correlation is found between λ_n and filament size pointing towards the role of the turbulence. The dependence of λ_n on Λ_{div} is weaker on TCV than on AUG and JET.

The MAST L-mode data rules out divertor detachment and the ionisation source as a reason for the density shoulder formation [68], in agreement with TCV L- and AUG H-mode data. Statistical analysis of data at different I_p showed that the size perpendicular to the flux surface (bi-normal), $\sigma_\perp$, decreases and the radial motion, $v_{b,r}$ of the filaments increases with $L_\parallel$ [67] without showing signs of a clear transition as on AUG or JET, despite the formation of a shoulder at low I_p. Given that a 50% reduction in $\sigma_\perp$ is observed alongside a five-fold increase in $L_\parallel$, the more

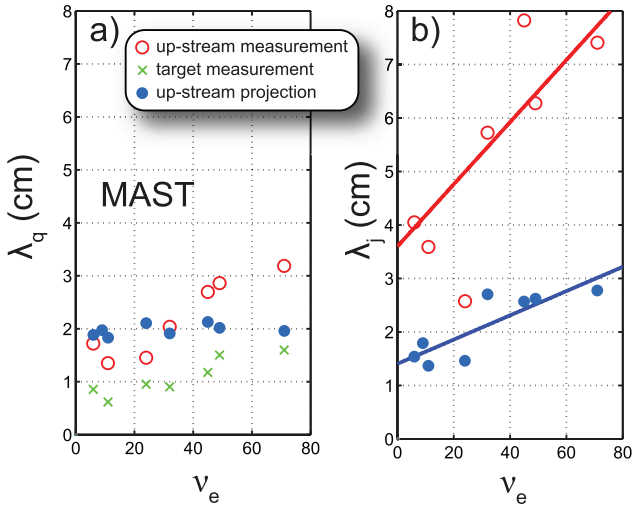

Figure 14. Comparison of up-stream and target (*a*) heat flux, (*b*) j_{sat} e-folding length in MAST as function of electron collisionality. Reproduced with permission from [68]. © 2016 EURATOM.

modest 100% increase in $v_{b,r}$ is substantially less than predicted by a sheath-dissipative scaling. Neither scaling predicts the observed change to $v_{b,r}$ which may be an indication that both inertial and sheath dissipative effects play a role in filament dynamics in MAST.

Another concern for future devices is the heat load to the limiters during start-up of the discharge. Heat flux profiles at the target of inboard limited L-mode plasmas are also found to be characterised by two scale lengths [74], with steeper gradients near the separatrix. Recent experiments in TCV are revealing that the near SOL gradients disappear at large normalised resistivity ($\nu \sim 10^{-2}$), which seems to correspond to the transition from the sheath-limited regime to the conduction-limited regime in the near SOL. It is seen that the power carried by the near SOL component is strongly correlated with the amplitude of non-ambipolar currents flowing to the limiters. Nonlinear global simulations of plasma dynamics for the TCV SOL are able to reproduce the near SOL steep gradients, though their strength appears weaker than in the experiments. This data may contribute to an international multi-machine scaling of λ_q in limiter discharges assembled recently projecting $\lambda_q^{\mathrm{imp}} = (57 \pm 14)$ mm for ITER [75]. It should be noted that the inter ELM heat flux width in AUG

and MAST scales like $\lambda_q \propto 1/B_{\mathrm{pol}}$ [76, 77] as observed also on other tokamaks [76], leading to predictions of a very narrow $\lambda_q^{\mathrm{ITER}} \approx 1$ mm on ITER for I_{p}15 MA [76] in deuterium. This data set will be extended by TCV data in the future.

Comparing upstream SOL profiles from various measurements with target profiles [66, 68] showed that projecting target values to up-stream values using a drift-based model [78] works well for the heat flux width λ_q, but is not appropriate for the saturation current (see figure 14). Indeed the heat flux carried by the filaments in the wings of the profile is only a small fraction of the total power balance [66]. The filamentary dynamics in the mid-plane are found to be compatible with an established scaling of the heat flux width λ_q.

7. Summary and outlook

Research on EU-MST has improved our understanding towards an integrated plasma-edge/wall solution. Critical questions such as ELM control, small ELM regimes, detachment control, operation in He, advanced divertor configurations and cross field SOL transport have been progressed considerably. ELM suppression has been achieved at low collisionality for the first time on AUG and the transferability of RMP ELM control from He to D has been shown. The modelling of the plasma response has been validated with several different codes. The role of the SOL density for access to small ELM regimes has been demonstrated, unifying pictures at high gas fuelling and application of RMP. In particular, the ITER base-line scenario has been shown to be close to the access to small ELM regimes. Future work needs to prove that such regimes are indeed possible with high SOL density, but low collisionality. The advanced divertor configurations start questioning the validity of our understanding of SOL transport. Modelling of the closed MAST-U divertor shows very promising reduction in target heat loads, but also stresses the importance of divertor closure. Filamentary transport leads to the formation of a broad density shoulder. Far SOL heat loads, however, seem to be only a fraction of the total power balance. The shoulder formation is clearly governed by a change in turbulent behaviour, but a unifying parameter characterising this transition has not been found yet.

Despite the considerable progress achieved many open questions still remain. The importance of this issue is reflected by two of the top three priorities for the future EU-MST1 programme, namely:

- Explore the applicability of type-II/grassy and RMP suppressed ELM regimes, as well as I-mode [79] and QH mode [80], to ITER and DEMO with respect to SOL density, collisionality, metal wall compatibility and target heat and particle loads.
- Explore alternative scenarios making use of novel divertor configurations to reach high PB/R with acceptable power and particle loads.

In the plasma edge neutrals and atomic physics play a crucial role, and extrapolation to ITER and DEMO is difficult to achieve by experimental means such as scalings or dimensionless comparisons alone. A key issue for the future EU-MST programme is, therefore, the more and more detailed comparison between experiments and models over a broad parameter range. Also models have to be developed and benchmarked that accurately describe a 3D SOL. For this purpose, work is planned in the near future to port the ELM suppression regime to MAST-U and COMPASS. Accessing ELM suppression on further devices should help to identify the key physics ingredients needed for this regime and help in extrapolating it to ITER and DEMO. Similarly, effort is directed towards establishing similar small or no-ELM regimes on all three EU-MST devices, as well as having a coordinated effort on modelling these regimes. The availability of these regimes on devices with different size and parameter regimes will help to disentangle the roles of density and collisionality, which is key to understanding if these regimes are accessible to future devices. This is of particular importance for the high density small ELM regime (e.g. type-II like ELMs), which in current devices is lost at higher heating power.

With respect to the tolerable ELM heat loads, the data set currently contains only attached regimes, whilst ITER and DEMO have to operate with partial detachment. For type-I ELMs, where the power flux to the divertor is expected to re-attach the plasma, this may give a valid extrapolation; but for tolerable ELMs this may no longer be true. Therefore, it is important to extend the transient ELM heat load studies to partially detached regimes. In addition, the performance of the advanced divertor configurations has to be assessed with respect to these transient heat loads both under attached and detached conditions. Here, the stability of the configuration is also important, as ELMs also create perturbations in the edge current. From 2017 onwards MAST-U will contribute to this work with its closed divertor and the large variability of accessible divertor configurations. Furthermore, robust detachment control has to be developed with ITER and DEMO relevant observers and actuators. Here, also the effect impurities have on the overal confinement needs to be addressed. On the one hand, impurities are crucial to reducing the power flowing into the divertor. On the other hand, impurity accumulation in the core has to be avoided, and the effects of the impurities on overall confinement have to be understood. Injection of N or Ne have been found to improve pedestal stability and therefore plasma confinement [7, 81, 82] in metal wall devices.

For all of these studies the inherent multi-machine approach of the EU-MST programme is a strong advantage, as the same scientific teams naturally perform studies on the different devices.

Acknowledgments

This work has been carried out within the framework of the EUROfusion Consortium and has received funding from the Euratom research and training programme 2014–2018 under grant agreement No 633053. The views and opinions expressed herein do not necessarily reflect those of the European Commission.

References

[1] Zohm H. 1996 *Plasma Phys. Control. Fusion* **38** 105
[2] Kirk A. *et al* 2014 *Nucl. Fusion* **54** 114012
[3] Loewenhoff T. *et al* 2015 *Nucl. Fusion* **55** 123004
[4] Loarte A. *et al* 2003 *Plasma Phys. Control. Fusion* **45** 1549
[5] Schweinzer J. *et al* 2016 *Nucl. Fusion* **56** 106007
[6] Beurskens M. *et al* 2014 *Nucl. Fusion* **54** 043001
[7] Dunne M. *et al* 2017 *Plasma Phys. Control. Fusion* **59** 014017
[8] Stober J. *et al* 2001 *Nucl. Fusion* **41** 1123
[9] Eich T. *et al* 2016 *Proc. 22nd Int. Conf. on Plasma Surface Interactions in Controlled Fusion Devices (22nd PSI) (Rome, Italy, 30 May–3 June 2016)* (www.psi2016.enea.it)
[10] Sieglin B. *et al* 2016 Assessment of divertor heat load with and without external magnetic perturbation *Nucl. Fusion* **57** 066045
[11] Pitts R. *et al* 2013 *J. Nucl. Mater.* **438** S48
[12] Pitts R.A. 2016 private communication
[13] Kirk A. *et al* 2015 *Nucl. Fusion* **55** 043011
[14] Valovič M. *et al* 2016 *Nucl. Fusion* **56** 066009
[15] Leyland M. *et al* 2015 *Nucl. Fusion* **55** 013019
[16] Dunne M. *et al* 2017 *Plasma Phys. Control. Fusion* **59** 025010
[17] Lennholm M. *et al* 2015 *Nucl. Fusion* **55** 063004
[18] Suttrop W. *et al* 2017 *Plasma Phys. Control. Fusion* **59** 014049
[19] Leuthold N. *et al* 2017 *Plasma. Phys. Control. Fusion* **59** 055004
[20] Osborne T.H. *et al* 1997 *Europhysics Conf. Abstracts (Proc. 24th EPS Conf. on Controlled Fusion and Plasma Physics (Berchtesgaden, 1997))* ed W. Schittenhelm *et al* vol 21A, part III, pages 1101–5, EPS secretariat, 6 rue des Frères Lumière 68200 Mulhouse France, European Physical Society
[21] Liu Y. *et al* 2016 *Nucl. Fusion* **56** 056015
[22] Ryan D.A. *et al* 2015 *Plasma Phys. Control. Fusion* **57** 095008
[23] Li L. *et al* 2016 *Nucl. Fusion* **56** 126007
[24] Ryan D.A. *et al* 2017 *Plasma Phys. Control. Fusion* **59** 024005
[25] Willensdorfer M. *et al* 2016 *Plasma Phys. Control. Fusion* **58** 114004
[26] Orain F. *et al* 2016 *Proc. 43rd EPS Conf. on Plasma Physics (Leuven, Belgium, 4–8 July 2016)* (*Europhysics Conf. Abstracts* vol 40A) (EPS) (http://ocs.ciemat.es/EPS2016PAP/html/)
[27] Mink F. *et al* 2016 *Proc. 43rd EPS Conf. on Plasma Physics (Leuven, Belgium, 4–8 July 2016)* (*Europhysics Conf. Abstracts* vol 40A) (EPS) (http://ocs.ciemat.es/EPS2016PAP/html/)
[28] Vanovac B. *et al* 2016 *Proc. 43rd EPS Conf. on Plasma Physics (Leuven, Belgium, 4–8 July 2016)* (*Europhysics Conf. Abstracts* vol 40A) (EPS) (http://ocs.ciemat.es/EPS2016PAP/html/)
[29] Suttrop W. *et al* 2011 *Phys. Rev. Lett.* **106** 225004
[30] Wolfrum E. *et al* 2015 *42nd EPS Conf. on Plasma Physics (Lisbon, Portugal, 22–26 June 2015)* (*Europhysics Conf. Abstracts* vol 39E) (European Physical Society) (http://ocs.ciemat.es/EPS2015PAP/html/)
[31] Lang P. *et al* 2013 *Nucl. Fusion* **53** 043004
[32] Kocsis G. *et al* 2015 *42nd EPS Conf. on Plasma Physics (Lisbon, Portugal, 22–26 June 2015) (Europhysics Conf. Abstracts* vol 39E) (European Physical Society) (http://ocs.ciemat.es/EPS2015PAP/html/)
[33] Schneider P.A. *et al* 2014 *Plasma Phys. Control. Fusion* **56** 025011
[34] Frassinetti L. *et al* 2017 *Nucl. Fusion* **57** 022004
[35] Kirk A. *et al* 2008 *J. Phys.: Conf. Ser.* **123** 012012
[36] Evans T.E. *et al* 2004 *Contrib. Plasma Phys.* **44** 235
[37] Bernert M. *et al* 2015 *Plasma Phys. Control. Fusion* **57** 014038
[38] Kallenbach A. *et al* 2010 *Plasma Phys. Control. Fusion* **52** 055002
[39] Bernert M. *et al* 2016 *Proc. 22nd Int. Conf. on Plasma Surface Interactions in Controlled Fusion Devices (22nd PSI) (Rome, Italy, 30 May–3rd June)* (https://doi.org/10.1016/j.nme.2016.12.029)
[40] Reimold F. *et al* 2016 *Proc. 22nd Int. Conf. on Plasma Surface Interactions in Controlled Fusion Devices (22nd PSI) (Rome, Italy, 30 May–3rd June)* (https://doi.org/10.1016/j.nme.2017.01.010)
[41] Faitsch M. *et al* 2016 *Proc. 22nd Int. Conf. on Plasma Surface Interactions in Controlled Fusion Devices (22nd PSI) (Rome, Italy, 30 May–3rd June)*
[42] Nardon E. *et al* 2011 *J. Nucl. Mater.* **415** S914
[43] Thornton A. *et al* 2014 *Nucl. Fusion* **54** 064011
[44] Jakubowski M. *et al* 2009 *Nucl. Fusion* **49** 095013
[45] Jia M. *et al* 2016 *Plasma Phys. Control. Fusion* **58** 055010
[46] Harting D. *et al* 2012 *Nucl. Fusion* **52** 054009
[47] Ahn J.-W. *et al* 2010 *Nucl. Fusion* **50** 045010
[48] Frerichs H. *et al* 2015 *Phys. Plasmas* **22** 072508
[49] Brida D. *et al* 2016 *Proc. 22nd Int. Conf. on Plasma Surface Interactions in Controlled Fusion Devices (22nd PSI) (Rome, Italy, 30 May–3rd June)*
[50] Sanchis-Sanchez L. *et al* 2016 *Proc. 43rd EPS Conf. on Plasma Physics (Leuven, Belgium, 4–8 July 2016) (Europhysics Conf. Abstracts* vol 40A) (EPS) (http://ocs.ciemat.es/EPS2016PAP/html/)
[51] Garcia-Munoz M. *et al* 2016 *Preprint 2016: IAEA Fusion Energy Conf. (Kyoto, Japan, 17–22 October)* (www-pub.iaea.org/iaeameetings/48315/26th-IAEA-Fusion-Energy-Conference)
[52] Kurki-Suonio T. *et al* 2017 *Plasma Phys. Control. Fusion* **59** 014013
[53] Theiler C. *et al* 2017 *Nucl. Fusion* **57** 072028
[54] Reimerdes S. *et al* 2016 TCV experiments towards the development of a plasma exhaust solution *Preprint: 2016 IAEA Fusion Energy Conf. (Kyoto, Japan, 17–22 October)* [EX/2-3]
[55] Havlíčková E. *et al* 2014 *Plasma Phys. Control. Fusion* **56** 075008
[56] Havlíčková E. *et al* 2015 *Plasma Phys. Control. Fusion* **57** 115001
[57] Lunt T. *et al* 2016 *Plasma Phys. Control. Fusion* **58** 045027
[58] Labit B. *et al* 2016 *Proc. 22nd Int. Conf. on Plasma Surface Interactions in Controlled Fusion Devices (22nd PSI) (Rome, Italy, 30 May–3rd June)*
[59] Canal G. *et al* 2015 *Nucl. Fusion* **55** 123023
[60] Verhaegh K. *et al* 2016 *Proc. 22nd Int. Conf. on Plasma Surface Interactions in Controlled Fusion Devices (22nd PSI) (Rome, Italy, 30 May–3rd June)*
[61] Harrison J. *et al* 2016 *Proc. 22nd Int. Conf. on Plasma Surface Interactions in Controlled Fusion Devices (22nd PSI) (Rome, Italy, 30 May–3rd June)* (https://doi.org/10.1016/j.nme.2016.10.020)
[62] Labombard B. *et al* 2001 *Phys. Plasmas* **8** 2107
[63] Carralero D. *et al* 2016 *Proc. 22nd Int. Conf. on Plasma Surface Interactions in Controlled Fusion Devices (22nd PSI) (Rome, Italy, 30 May–3rd June)* (https://doi.org/10.1016/j.nme.2016.11.016)
[64] Carralero D. *et al* 2015 *Phys. Rev. Lett.* **115** 215002
[65] Carralero D. *et al* 2016 Recent progress towards a quantitative description of filamentary SOL transport *Nucl. Fusion* **57** 056044
[66] Thornton A.J. *et al* 2015 *Plasma Phys. Control. Fusion* **57** 115010
[67] Kirk A. *et al* 2016 *Plasma Phys. Control. Fusion* **58** 085008
[68] Militello F. *et al* 2016 *Nucl. Fusion* **56** 016006
[69] Militello F. *et al* 2016 ITER fuelling requirements and scenario development for H, He and DT through JINTRAC

integrated modelling *Preprint: 2016 IAEA Fusion Energy Conf. (Kyoto, Japan, 17–22 October)* [TH/P2-23]
[70] Vianello N. *et al* 2016 On filamentary transport in the TCV tokamak: addressing the role of the parallel connection length *Preprint: 2016 IAEA Fusion Energy Conf. (Kyoto, Japan, 17–22 October)* [EX/P8-26]
[71] Müller H. *et al* 2015 *J. Nucl. Mater.* **463** 739
[72] Allan S.Y. *et al* 2016 *Plasma Phys. Control. Fusion* **58** 045014
[73] Theiler C. *et al* 2009 *Phys. Rev. Lett.* **103** 065001
[74] Labit B. *et al* 2016 The physics of the heat flux narrow decay length in the TCV scrape-off layer: experiments and simulations *Preprint: 2016 IAEA Fusion Energy Conf. (Kyoto, Japan, 17–22 October)* [EX/P8-25]
[75] Horacek J. *et al* 2015 *J. Nucl. Mater.* **463** 385
[76] Eich T. *et al* 2013 *Nucl. Fusion* **53** 093031
[77] Harrison J. *et al* 2013 *J. Nucl. Mater.* **438** S375
[78] Eich T. *et al* 2011 *Phys. Rev. Lett.* **107** 215001
[79] Ryter F. *et al* 2017 *Nucl. Fusion* **57** 016004
[80] Burrell K.H. *et al* 2016 *Phys. Plasmas* **23** 056103
[81] Kallenbach A. *et al* 2016 Overview of ASDEX Upgrade results *Nucl. Fusion* **57** 102015
[82] Stefanikova E. *et al* 2016 *43rd EPS Conf. on Plasma Physics (Leuven, Belgium, 4–8 July 2016) (Europhysics Conf. Abstracts* vol 40A) (EPS) (http://ocs.ciemat.es/EPS2016PAP/pdf/O4.117.pdf)
[83] Bernert *et al* 2017 Power exhaust by SOL and pedestal radiation at ASDEX Upgrade and JET M J. *Nucl. Mater. Energy* (https://doi.org/10.1016/j.nme.2016.12.029)
[84] Reimerdes H. *et al* 2017 TCV Experiments towards the Development of a Plasma Exhaust Solution *Nucl. Fusion* submitted